Journal of Biomedical Optics

BiomedicalOptics.SPIEDigitalLibrary.org

Review of the state of the art in cardiovascular endoscopy imaging of atherosclerosis using photoacoustic techniques with pulsed and continuous-wave optical excitations

Sung Soo Sean Choi
Andreas Mandelis

SPIE.

Sung Soo Sean Choi, Andreas Mandelis, "Review of the state of the art in cardiovascular endoscopy imaging of atherosclerosis using photoacoustic techniques with pulsed and continuous-wave optical excitations," *J. Biomed. Opt.* **24**(8), 080902 (2019), doi: 10.1117/1.JBO.24.8.080902.

Journal of Biomedical Optics 24(8), 080902 (August 2019)

REVIEW

Review of the state of the art in cardiovascular endoscopy imaging of atherosclerosis using photoacoustic techniques with pulsed and continuous-wave optical excitations

Sung Soo Sean Choi and Andreas Mandelis*
University of Toronto, Center for Advanced Diffusion-Wave and Photoacoustic Technologies, Department of Mechanical and Industrial Engineering, Toronto, Ontario, Canada

Abstract. Intravascular photoacoustics (IV-PA) is an emerging atherosclerosis imaging modality that provides chemical-specific optical information of arterial walls with acoustic depth penetration and resolution. As lipid composition of atherosclerotic plaques is considered to be one of the primary indicators for plaque vulnerability, many IV-PA applications are calibrated so as to target plaque necrotic cores. Based on the mode of optical excitation and the corresponding signal processing technique, IV-PA is categorized into two different modalities. The pulse-based IV-PA has been the universal IV-PA imaging mode with its high peak power and straightforward time-domain signal processing technique. As an alternative, the low power continuous-wave (CW)-based IV-PA has been under intense development as a radar-like frequency-domain signal processing modality. The two state-of-the-art types of IV-PA are reviewed in terms of their physics and imaging capabilities, with major emphasis on frequency-swept CW-based IV-PA that has been recently introduced in the field. [DOI: 10.1117/1.JBO.24.8.080902]

Keywords: photoacoustic imaging; endoscopy; atherosclerosis; time-domain; frequency-domain.

Paper 190148VR received May 8, 2019; accepted for publication Jul. 22, 2019; published online Aug. 14, 2019.

1 Introduction: Atherosclerosis and Conventional Imaging Modalities

Atherosclerosis is a subcategory of cardiovascular disease (CVD) characterized by inflammation and the gradual buildup of lipid-rich plaque in the inner lining of the arterial walls (tunica intima).[1–4] This disease is critical as it is directly responsible for other types of more serious CVD, such as coronary heart disease and stroke, and therefore death. While the full risk factors or the cellular mechanism of plaque development are not yet fully understood, the development of plaques is known to self-accelerate, developing size and intramural calcification while compromising the luminal elasticity.[5–7]

Although an affected artery may show no sign of disease for decades, growing plaques may result in partial or complete occlusion of a lumen. Such luminal narrowing (stenosis) contributes to clinical manifestations of serious CVD to a certain degree; however, it is mainly the superimposition of an arterial thrombus over a ruptured plaque that causes most of the acute coronary syndromes (ACS).[5] In other words, atherosclerosis becomes dangerous when plaques rupture and cores release thrombogenic contents into the bloodstream.[8–11] Plaques with a higher risk of rupture are generally referred to as "unstable" or "vulnerable."[5,12] While there are a few subcategories of vulnerable plaques, clinical studies characterize vulnerable plaques as having a large volume of necrotic core (>40% plaque volume) with an overlying fibrous cap measuring <65 μm, a small degree of stenosis (<50% diameter narrowing), and mostly occurring in the proximal coronary artery.[5,12–20] Nonetheless, definite triggers for sudden rupture of vulnerable plaques remain to be explored.[21–23] While plaques can rupture spontaneously, it should be acknowledged that not all plaque ruptures would cause life-threatening ACS.[24] In those silent ruptures, thromboses may become successfully regulated and eventually lead to regression.

A useful frontline and today's gold-standard diagnostic technique to assess progression of atherosclerosis is an invasive x-ray angiogram.[25–27] With its superior resolution of ~100 μm, an x-ray angiography scan indirectly detects plaques by locating stenosis and luminal irregularities while substantially lacking morphological and compositional information of plaques.[25,26] Intravascular ultrasound (IVUS) is a catheter-based imaging technique that utilizes an oscillating sound pressure wave with frequencies in the 20- to 60-MHz range to detect a mechanical anomaly within the imaging environment.[25] In addition to its superior resolution in deep biological tissue, IVUS has been declared by the World Health Organization (WHO) as a safe screening tool for the public without any known short-term or long-term side effects.[28] However, IVUS produces gray-scale images with poor mechanical contrast, and it may not differentiate plaque constituents.[25,29] Further development of IVUS which performs a spectral analysis of the backscattered radio-frequency (RF) data was developed as virtual histology IVUS (VH-IVUS).[25] While VH-IVUS demonstrated the capability to differentiate a necrotic core, calcium, and lipid,[30] its accuracy and consistency are still being questioned.[31,32] Intravascular optical coherence tomography (OCT) is another well-developed catheter-based imaging modality for atherosclerosis evaluation. It is analogous to IVUS, but instead of utilizing acoustic signals, it employs nonionizing electromagnetic radiation (EMR) in the

*Address all correspondence to Andreas Mandelis, E-mail: mandelis@mie.utoronto.ca

near-infrared (NIR) region to obtain backscattered or backreflected photons to extract optical information.[33] OCT signal detection depends on wavelength-specific optical scattering of tissue, and therefore, OCT produces images with superior contrast even when suspicious atherosclerotic regions are not anatomically obvious. It presents an exceptionally high spatial resolution of $\sim 10\ \mu$m and can differentiate different plaque types accurately based on their optical properties.[34] However, the imaging depth of OCT is strictly limited to ~ 1 mm due to optical scattering through heterogeneous tissue, and it makes the assessment of relatively thick plaque challenging.[25,33,34] Furthermore, OCT still requires an extra step of blood substitution by an optically clear solution which makes the imaging procedure rather unfavorable.

2 Intravascular Photoacoustic Imaging in Atherosclerosis

2.1 *Principles of IV-PA Imaging*

One of the latest techniques introduced in this field of plaque evaluation is intravascular photoacoustic (IV-PA) imaging. IV-PA is a catheter-based imaging technique that partially resembles IVUS and OCT in terms of its hardware design. As a promising optical-acoustic hybrid imaging modality based on the use of laser-generated ultrasound, the contrast of IV-PA is based on the optical absorption difference between a target chromophore and surrounding tissues while the generated information is encoded and carried in the form of acoustic signals. Therefore, IV-PA imaging combines the high contrast of optical imaging, and deep subsurface-penetration and high spatial resolution of acoustic imaging, without suffering from the major drawbacks of each technique. The theory behind IV-PA is the "photoacoustic (PA) effect."[35] The PA effect explains the chain of the energy conversion process from EMR to acoustic pressure waves as shown in Fig. 1.

Most IV-PA systems today employ optical sources in the NIR spectral region to facilitate imaging in the presence of blood, and consequently, deeper penetration is realizable to cover the full thickness of a plaque. In addition, direct detection of lipids is very likely within this region as the absorption spectrum of lipids is well differentiated from other plaque chromophores, particularly at ~ 1210 and ~ 1700 nm due to the second and the first overtone of C-H bond vibrations within lipid molecules,

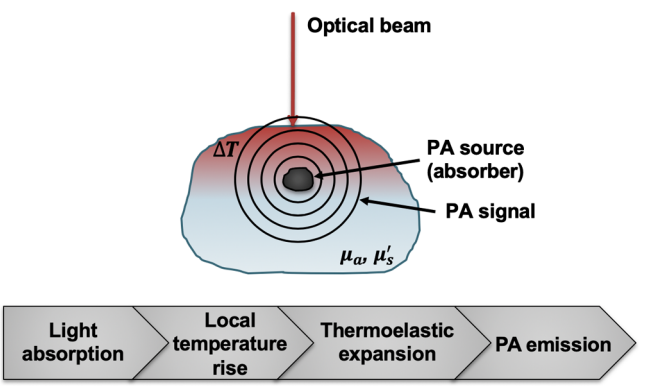

Fig. 1 Illustration of the sequential energy conversion processes of the PA effect. μ_a, the absorption coefficient of an absorber; μ_s', the reduced scattering coefficient of surrounding tissue; ΔT, local temperature change of an absorber.

respectively.[36–39] IV-PA is also regularly integrated with other popular endoscopic imaging modalities such as IVUS and OCT in order to further improve its imaging capability.[40–43] Especially, coregistration with IVUS is very easy to implement as IV-PA and IVUS share the same endoscopic transducer.

In order to induce meaningful PA signal conversion at absorbers, it is important to acknowledge that the intensity of the illuminating light must be pulsed or modulated in a specific pattern.[35,44] Throughout the described optical-to-acoustic energy conversion processes, the evolved acoustic waves exhibit the same modulation pattern as the excitation optical beam. Regardless of the modulation patterns of the optical source, it is the wavelength-dependent optical properties of PA targets and surrounding tissues that mainly govern the efficiency of PA signal generation. While the most important optical property for PA imaging is the absorption coefficient, μ_a, others such as the scattering coefficient, μ_s, and the anisotropy factor, g,[45–47] also affect the overall PA signal generation by controlling the number of photons available for absorption.

Once PA signals are induced, the efficiency of PA detection is partly governed by the frequency-dependent acoustic attenuation coefficient of inhomogeneous media, along with the transfer function of a transducer. Acoustic attenuation in tissue, α_s', is considered to have a linear frequency dependence as $\alpha_s' = \alpha_s f$, while it is highly negligible at low frequencies below ~ 1 MHz.[48] Another important acoustic property in PA imaging is the speed of sound in the medium, c_a. While c_a is determined by the density and compressibility of the medium, the mean speed of sound in water (≈blood) and human soft tissue is ~ 1500 m/s or 1.50 mm/μs.[49]

2.2 *General Designs of IV-PA Catheter Systems*

Figure 2 shows a few design examples of typical IV-PA catheter systems. Some designs rely on a polished optical fiber (at 33°C to 37.5°C) to deliver the beam to an arterial wall at an angle via total internal reflection.[50–55] A small endoscopic transducer is placed below the optical fiber so that it aligns with the area of light and tissue interaction in front of it. Many other designs utilize an angled mirror or a prism to direct the beam to an arterial wall and implement an optically transparent acoustic mirror to transmit generated acoustic signals back to a transducer in a catheter.[42,56,57] Lastly, some other popular designs employ a transducer with a hole at the center (ring-shaped).[40,41,58] In this case, the laser beam is directed through the hole so that the travel paths of light and sound are overlapped as much as possible while compromising detection sensitivity of the transducer to some extent.

For optical collimating and focusing purposes, some catheter designs incorporate small optics inside. A graded-index (GRIN) lens and an aspheric lens are typical choices to achieve stationary focusing[42,57] while a use of a liquid lens was recently reported for dynamic focusing.[58] For mechanical rotation of a catheter, a flexible torque cable and a rotary motor are usually employed.[50,51,56,57] Such variations in the IV-PA catheter design were shown to pose different challenges for *in vivo* demonstration of the system such as the large catheter diameter (larger than ~ 1 mm), PA/US resolution loss due to multiple reflective optics, and unsynchronized PA/US imaging field.[59,60] Regardless of the details, the ultimate objective of different catheter designs is to deliver the light to a target area that is parallel to a catheter body and to transmit the generated PA signal to an enclosed detector.

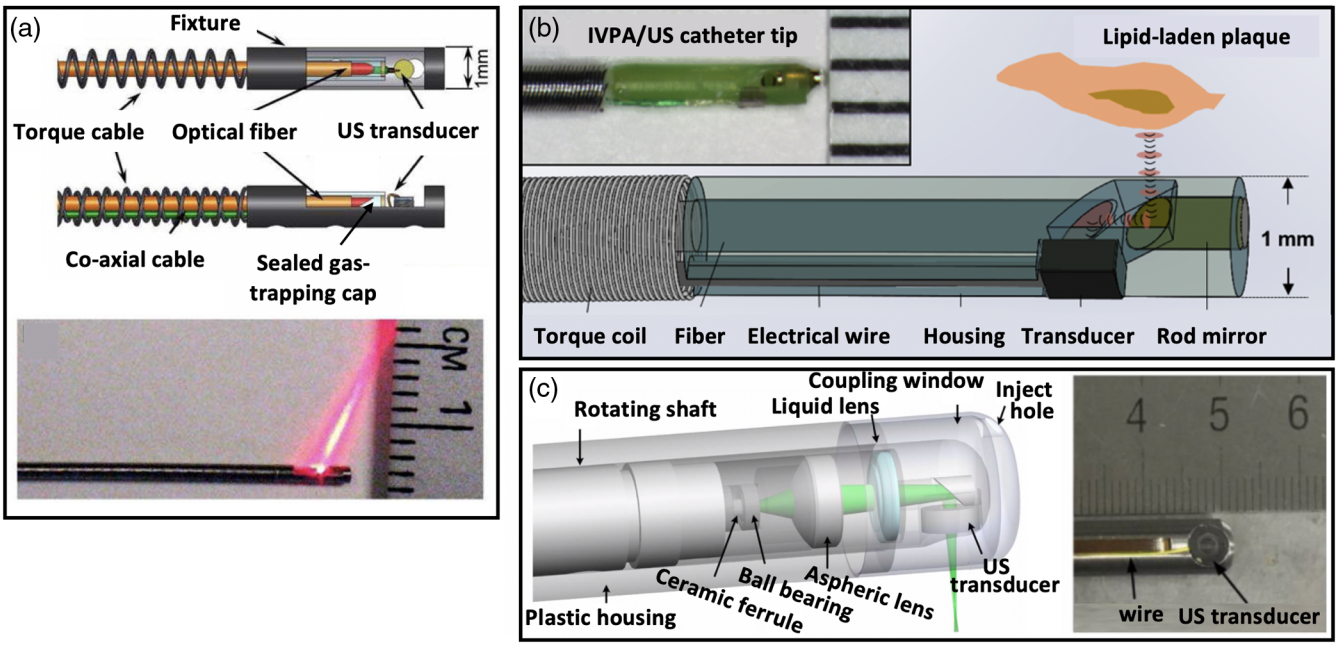

Fig. 2 Design examples of general IV-PA catheter tip. Each design achieves light and sound alignment by using (a) a polished fiber, (b) an optically transparent acoustic mirror, and (c) a ring-shaped transducer. Reproduced with permission from Refs. 51, 56, and 58.

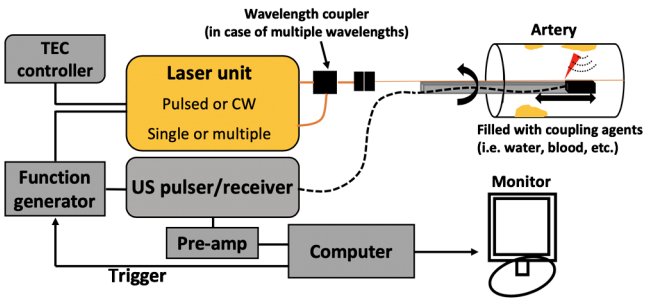

Fig. 3 Block diagram of typical IV-PA imaging set-up. Depending on the type of IV-PA, the details of the laser unit and the corresponding light delivery system may vary. CW, continuous wave.

The typical imaging set-up of IV-PA is shown in Fig. 3, where coregistration of IV-PA and IVUS is readily facilitated.

Recently, much interest was raised in developing real-time IV-PA systems. Numerous studies demonstrated fast assessment of plaques by employing the optical source with pulse repetition rate in the kHz range.[51,56,59,60] Specifically, Vander Laan et al.[51] reported a real-time IV-PA/IVUS imager with ~30 frames per second (FPS) by improving the efficiency of digitization. Similarly, Hui et al.[56] reached ~25 FPS for IV-PA/IVUS imaging with their differentiated A-line strategy where triggering frequencies of IV-PA and IVUS were engineered. As demonstrated by those reports, careful optimization is needed in both hardware and software in order to achieve a faster imaging speed toward reliable real-time monitoring of atherosclerosis.

3 Two Types of Intravascular Photoacoustic Imaging Modality

3.1 *Pulse-Based and CW-Based IV-PA*

Depending on the mode of radiation, an optical source for general IV-PA imaging can be categorized into pulsed laser and continuous-wave (CW) types. The former provides a train of high-power ns-long optical pulses while the latter provides low-power but high modulation-frequency continuous optical beam to excite chromophores.[35,44] A periodically modulated single-frequency CW optical source was used in the original discovery of the PA effect and has been widely used for various spectroscopic studies.[35,44] However, the former has been the exclusive type of an optical source for various bench-top and preclinical PA imaging applications since the very early stages of biomedical PA research.[61,62] It can induce acoustic transients with large magnitude using relatively less complicated time-domain (TD) signal processing algorithms that allow a straightforward depth determination from time-of-flight measurements with great computational efficiency.[63–65] However, they may not be easily transferred to clinical environments due to their large footprint and high cost. In addition, pulse-based PA systems cannot be tuned flexibly for different needs because the important system parameters, such as power, pulse repetition frequency, and signal apodization, are predefined.[49] They also require regular maintenance and sensitive calibration by trained professionals for optimal performance. While a recent study on laser threshold in IV-PA suggested that pulsed lasers can be safe to use by varying the imaging protocol (at the expense of image quality),[66] its high peak power may also raise some safety concerns of exceeding the laser maximum permissible exposure (MPE) level and damaging tissue.[49] In terms of signal detection, pulse-based IV-PA systems require very sensitive transducers with extremely wide bandwidth (>40 MHz) in order to achieve sufficient signal-to-noise ratio (SNR).[67,68] For such wideband detection, more noise would contribute at the receiving end, compromising SNR. Lastly, laser jitter noise and the bipolar shape of pulsed PA transients that are caused by photon-transducer interaction, compressions, and rarefaction, respectively, have an adverse effect on the spatial resolution and contrast of the system which can eventually distort resulting images.

Acknowledging such limitations of the pulse-based IV-PA, single-frequency-modulated CW-based IV-PA was revisited as a potential alternative. The development of a portable IV-PA imager for the clinical environment is much more likely with CW optical sources due to the wide availability of compact and low-cost diode sources in the NIR spectrum. Furthermore, its low peak power is beneficial for clinical uses compared to its pulsed counterparts as a tissue is exposed to much lower photon energy. In this conventional CW-based IV-PA, however, the magnitude of the resulting PA signals is very small, and this has been the primary factor preventing the development of this method in the field.[67] In addition, due to its extremely narrow bandwidth, this method lacked depth-resolved information of targets, therefore not being suitable for intravascular imaging.[49,67]

In mid 2010, advancement in the CW-based IV-PA started to appear in the field, implementing frequency-swept (intensity-modulated) optical modulation and the frequency-domain (FD) matched-filter pulse compression signal processing algorithm[52–55] that was originally explored in the radar/sonar technologies.[48,49,67–79] As signal outputs of this modality are represented by an arbitrary correlation unit which is determined by the total spectral energy of signals, they are not directly comparable with pressure signals of the aforementioned pulse-based IV-PA modalities. However, the compressed PA signals in this mode offer very high SNR that may compensate for the weak pressure magnitude of the raw acoustic signals. As summarized in Table 1, a few experimental comparative studies between pulse-based and frequency-swept CW-based PA modalities demonstrated that the CW-modality is highly competitive to its conventional pulse-based counterpart, providing comparable or even better SNR, resolution, similar maximum imaging depth, and depth-resolved/molecularly specific optical contrast of the subsurface absorber, while utilizing low power irradiation and narrowband detector.[49,72]

Most importantly, the CW-based IV-PA method is flexible in that the system parameters such as linear frequency modulation (LFM) chirp waveform, duration, and bandwidth are fully

Table 1 Comparison between pulse-based and frequency-swept CW-based FD PA.

	Pulse-based PA	CW-based FD PA	Ref.
Optical source	1064-nm Q-switched laser (5 ns duration with 10 Hz repetition)	1064-nm CW and acousto-optic modulator (AOM)	72
Fluence or Intensity	~10 mJ/cm^2	~9.5 W/cm^2	
Sample	Phantom with $\mu_a = 6$ cm^{-1} in 0.47% intralipid solution		
Detector	3.5 MHz (focused)	0.5 MHz (focused)	
Maximum depth	18 to 23 mm	~25 mm	
Estimated maximum depth[a]	35 to 45 mm	32 to 38 mm	
Optical source	1064-nm Q-switched laser (5 ns duration with 10 Hz repetition)	1064-nm CW and AOM	49
Fluence or Intensity	~100 mJ/cm^2	~6.5 W/cm^2	
Sample	Black rubber at a depth of 16 mm in 0.47% intralipid solution		
Detector	0.5 MHz (focused)		
CF[b]	2.4	3.7	
SNR	11.8 dB	23.1 dB	
Axial resolution	0.86 μs	2.43 μs	
Detector	3.5 MHz (focused)		
CF[b]	3.1	3.8	
SNR	2.61 dB	23.2 dB	
Axial resolution	0.164 μs	0.46 μs	
Sample	Phantom with $\mu_a = 4$ cm^{-1} in 0.47% intralipid solution		
Detector	3.5 MHz (focused)		
Maximum depth	22 mm	18 mm	

[a]By assuming efficient signal conditioning to suppress the background interference signal.
[b]Contrast factor (CF) is calculated by dividing the differences of mean signal in the absorber and background by mean signal in the background.

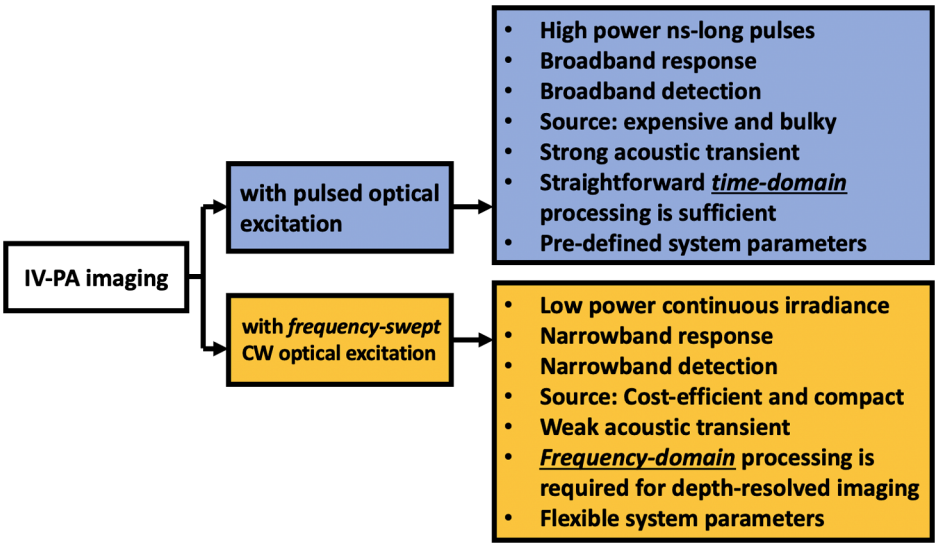

Fig. 4 Brief outlook on pulse-based TD IV-PA and frequency-swept CW-based FD IV-PA imaging techniques. While the energy conversion principles of PA signal generation are similar, the two systems differ in both hardware and software.

controllable by an operator.[48,49,52–55,71–73] Such system flexibility allows various waveform-engineered designs of the modulating optical signals that can lead to several unique or enhanced imaging features such as depth-selective and differential IV-PA imaging reviewed here. Figure 4 shows a few fundamental differences between pulse- and frequency-swept CW-based IV-PA modes.

3.2 *Generation of Pulse-Based PA Signals*

The PA response from a pulsed optical source can be described by the wave equation for pressure at point r at time t, $p(r,t)$[67]

$$\nabla^2 p(r,t) - \frac{1}{c_a^2}\frac{\partial^2}{\partial_t^2} p(r,t) = -\frac{\beta}{C_p}\frac{\partial}{\partial_t} q(r,t), \tag{1}$$

$$q(r,t) = \mu_a(r)\phi(r;\mu_a,\mu_s,g)\delta(t), \tag{2}$$

where β is the isobaric volume thermal expansivity; C_p is the specific heat capacity for constant volume; $q(r,t)$, the source function in Eq. (2), is the density of optical energy per unit time deposited at position r with corresponding μ_a and μ_s over the illuminated tissue volume; $\phi(r)$ is the optical fluence at r; and $\delta(t)$ is the Dirac delta function. As $q(r,t)$ is a function of the optical fluence, it is normally estimated by exponential attenuation.[48] The general solution of Eq. (1) is given by an integral of Green's function. Considering the optical attenuation due to light diffusion, the acoustic pressure at a point of transducer r_t, $p(r_t)$, can be described as[62,67]

$$p(r_t) = \frac{\Gamma\alpha H(r_s)}{2|r_t - r_s|} = \frac{\Gamma\mu_a(r_s)\alpha\phi(r_s;\mu_a,\mu_s,g)}{2|r_t - r_s|}, \tag{3}$$

$$\Gamma = \beta\frac{c_a^2}{C_p}, \tag{4}$$

where Γ is the Grüneisen coefficient which is a dimensionless constant that describes the efficiency of thermoacoustic excitation, α is the radius of a PA source, r_s is the location of a PA source, and $H(r_s)$ is the absorbed optical energy distribution at a PA source which is given by the product of the local absorption coefficient and the optical fluence. Even though the overall effects of thermodynamic properties of tissue on the generated acoustic signals are described by the Grüneisen coefficient in Eq. (4), it is usually assumed in PA imaging that the Grüneisen coefficient is relatively constant in different tissue types.[62] Therefore, Eq. (3) indicates that PA signal generation is highly dominated by the optical properties of a PA source, especially μ_a. It should be acknowledged, however, that resulting PA signals are not linearly proportional to μ_a, but instead, they possess a nonlinear relationship due to the effect of absorption-dependent optical fluence.[62] In Eq. (3), the time variable is not considered anymore as the corresponding optical irradiation is short and therefore negligible. Excited by high-power δ-like optical pulses, generated acoustic signals with high magnitude propagate away from a PA source. The delay time, τ, between optical excitation and acoustic wave arrival can be evaluated as the depth of a PA source, r, as it is preserved as $r = c_a\tau$. This time-of-flight estimation is simple but assumes c_a to be frequency-independent. In other words, this approach is reliable when background media are relatively nondispersive. In this case, the shape of resulting PA signals would highly resemble wide-band δ-like optical pulses and τ can be accurately measured by evaluating their peaks. However, if media are dispersive to some extent, which is the case for most biological tissues, evaluating τ becomes challenging as the shape of PA signals gets distorted as they travel toward a detector. As the acoustic attenuation in tissue is considered to have a linear frequency dependency, this relationship can be used for accurate interpretation of PA magnitude through normalization.[49] Equation (5) then can be used to inversely solve μ_a from the corresponding acoustic signals, but low SNR from wide-band detection and the above-mentioned signal distortion during propagation may compromise the accuracy of such measurements.[67]

3.3 *Generation of Conventional CW-Based PA Signals*

When single-frequency-modulated CW optical energy is absorbed by imaging targets, corresponding frequency-modulated acoustic

waves are generated and propagate away from a source. These waves can be expressed in FD and are directly related to the TD wave equation that was described in Eq. (1). By utilizing Fourier transforms, the PA response from CW optical source can be described as[67]

$$\nabla^2\tilde{p}(r,\omega)+k^2\tilde{p}(r,\omega)=-\frac{i\omega\beta}{C_p}\tilde{q}(r,\omega), \tag{5}$$

where tilde denotes the Fourier transform representation, ω is the angular frequency, and k is the acoustic wave number defined as $k=\omega/c_a$. Similar to the TD representation, the general solution of Eq. (5) is given by an integral of Green's function and the acoustic pressure at r_t can be described as[67]

$$p(r_t,t)=\frac{|\tilde{p}(r_s,\omega)|}{4\pi|r_t-r_s|}e^{i\left[\omega\left(\frac{t-|r_t-r_s|}{c_a}\right)+\theta\right]}, \tag{6}$$

where $\tilde{p}(r_s,\omega)$ is the pressure amplitude at r_s at ω, and θ is the phase shift that takes place during the optical-to-acoustic energy conversion. Just like the described PA pressure in the pulse-based system, this signal is proportional to Γ, $\mu_a(r_s)$, and $\phi(r_s;\mu_a,\mu_s,g)$. Using Eqs. (3) and (6), Telenkov et al.[67] compared in simulation the peak pressure magnitude of pulse-based and single-frequency CW-based PA signals reaching a point transducer under similar measurement conditions. As expected, the pulse-based PA generated much stronger acoustic pressure (~1.6 Pa) than the CW mode (~0.002 Pa), about three orders of magnitude higher. This justified the use of pulsed optical sources as a standard mode of excitation in many PA studies and preclinical applications including IV-PA.[38–43,50,51,56,80–84]

3.4 *Intensity-Modulated CW-Based IV-PA Signal Generation and Processing*

Implementation of a coded input signal is the heart of the matched-filter pulse compression processing in this newly introduced method. With wider bandwidth than a single-frequency modulated source can provide, chirp modulation enables a bandwidth-dependent pulse compression algorithm that shrinks a relatively long acoustic signal into a narrow spike at the corresponding location of a subsurface chromophore. This, in turn, resolves the depth of a PA source by straightforward time-of-flight measurement that is typical to pulse-based PA modes. However, the principal difference between the two modalities must be highlighted. The FD pulse compression technique analyzes the entire record of a relatively long signal to identify the presence of signals with characteristics of the known reference signal, while pulse-based PA performs a single-point time-resolved measurement.[67,68,85]

There are many variables involved in optical modulation by a chirp waveform. For optimization of optical LFM waveform design in the CW-based PA modality, Lashkari and Mandelis[48] suggested doing so with respect to the maximum SNR of the processed signal. Based on their theoretical and the corresponding experimental studies, the optimal chirp bandwidth (BW_{ch}) did not necessarily have to be symmetric around the center frequency of a transducer. Especially in the MHz modulation range, the optimal BW_{ch} was shifted to a lower frequency range due to the combined effects of (1) decaying PA response over increasing frequency (low-pass filtering effect of PA energy conversion), (2) increasing acoustic attenuation over increasing frequency, and (3) rising portion of transducer transfer function below the center frequency. In addition to BW_{ch}, the time-bandwidth product, m,[67] and the shape of the excitation waveform itself[85] were shown to be critical in LFM optimization.

The block diagram of this intensity-modulated CW-based IV-PA signal processing algorithm is shown in Fig. 5(a).[54] Unlike pulse-based IV-PA that provides a single amplitude channel, CW-based IV-PA provides an additional correlation phase channel that is independent of the optical fluence.[54,86] This phase channel is usually represented in the form of its inverse standard deviation (ISDV) which correlates with the probability of the presence of PA sources at certain depths.[54] Then, such statistical information is encoded on the amplitude channel into phase-filtered amplitude (PFA) channel by simple multiplication. The PFA was demonstrated to further enhance SNR and axial resolution of target PA signals.[54] Figure 5(b) compares the SNR and axial resolution of the described CW-based IV-PA channels via computer simulation with a square chirp modulation in 1 to 5 MHz range and arbitrary random white Gaussian system noise with a factor of 100. From this comparison, the PFA channel showed ~125% and 29% improvement in its SNR and full-width at half-maximum axial resolution, respectively, compared to the corresponding amplitude channel by utilizing the same raw signal data.

3.5 *Intensity-Modulated CW-Based Differential IV-PA Signal Generation and Processing*

As briefly described above, the flexibility in system parameters of the CW-based IV-PA provides more room for further improvement in its imaging capability beyond the intrinsic physical limitation of conventional pulse-based PA systems.[54,55,87] In this regard, the differential IV-PA modality was recently reported as an extension of conventional CW-based IV-PA where many system parameters were carefully engineered for more accurate and reliable atherosclerotic plaque detection.[53–55,87] This differential method inherits the general traits of CW-based IV-PA in terms of signal generation and processing and therefore rely on the same signal processing algorithm described in Fig. 5(a).

Differential IV-PA uses the second wavelength in real time with identical chirp modulation at a specific optical phase difference, φ_{optical}. The relationship between the two modulating signals, $r_{\lambda_1}(t)$ and $r_{\lambda_2}(t)$, can be expressed as[87]

$$r_{\lambda_1}(t)=\text{sgn}\left[\sin\left(2\pi f_1 t+\frac{\pi \text{BW}_{\text{ch}}}{T_{\text{ch}}}t^2\right)\right],\quad -\frac{T_{\text{ch}}}{2}\le t\le\frac{T_{\text{ch}}}{2}, \tag{7a}$$

$$r_{\lambda_2}(t)=\text{sgn}\left[\sin\left(2\pi f_1 t+\frac{\pi \text{BW}_{\text{ch}}}{T_{\text{ch}}}t^2+\varphi_{\text{optical}}\right)\right],\quad -\frac{T_{\text{ch}}}{2}\le t\le\frac{T_{\text{ch}}}{2}, \tag{7b}$$

where $\text{sgn}(x)$ is the signum function, f_1 is the starting frequency, and T_{ch} is the total duration of an optical chirp waveform.

When the two coherent optical waves are simultaneously absorbed by an identical absorber, the two coherent acoustic pressure waves (s) are generated. Since the optical absorption coefficient of an absorber and corresponding PA signal generation process are wavelength-dependent, the two resulting raw PA signals may exhibit different magnitude and phase.[87]

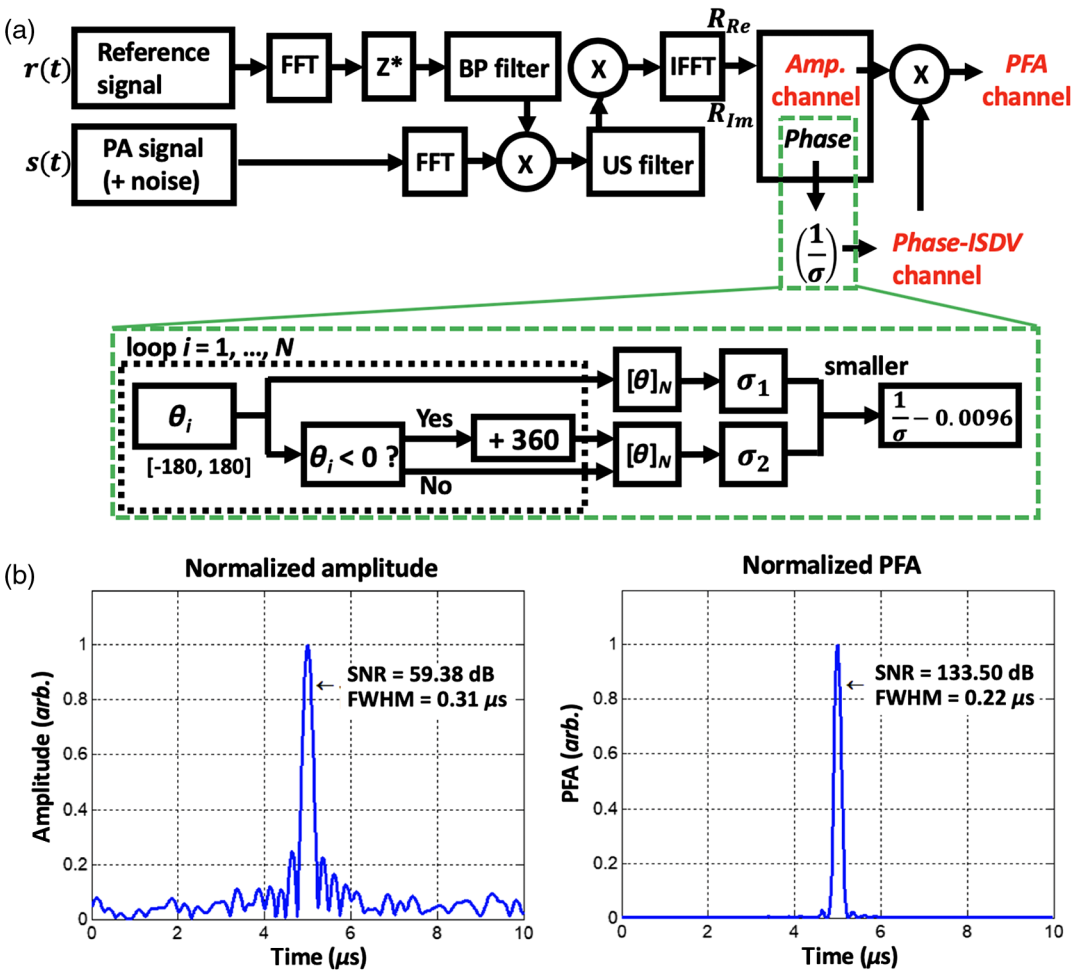

Fig. 5 (a) Block diagram of the matched-filter pulse compression signal processing algorithm of frequency-swept CW-based IV-PA. This process is similar to generating the analytic signal of an arbitrary signal in that it doubles positive frequency components while removing negative frequency components. FFT, fast Fourier transform; IFFT, inverse fast Fourier transform; Z^*, complex conjugate; Re, real component; Im, imaginary component; BP, bandpass filter; US, unit-step (Heaviside step function) filter; N, number of averaging signals; θ, phase; σ, standard deviation. For phase-ISDV channel, output value is linearly normalized by the constant to bring down the baseline. (b) Simulation example of CW-based IV-PA amplitude and PFA channels ($N = 50$). While square chirp modulation was assumed in 1 to 5 MHz range, arbitrary random white Gaussian noise was added to simulate a more realistic signal processing scenario. Reproduced with permission from Ref. 54.

Nonetheless, they are still coherent with a certain acoustic phase difference, $\varphi_{\text{acoustic}}$. These two acoustic waves are related to each other by spatial and temporal constants, and undergo stationary interference in the acoustic domain, resulting in a single differential PA signal upon generation. Depending on the selection of optical wavelengths and initial φ_{optical} between them, information carried by the resulting differential PA signals differ, but a general form of raw differential PA signals can be described as[87]

$$s_{\text{Diff}}(t) = s_{\lambda_1}(t) + s_{\lambda_2}(t). \tag{8}$$

In other words, the contents of differential PA signals are determined by the spontaneous interference between two single-ended PA signals in the acoustic domain. Therefore, the parameters of the differential IV-PA need to be selected carefully in order to encode the desired information in this differential PA channel.[87] The resulting PA signals at the time of detection need to contain only the cholesterol-derived information without any contribution from other types of adjacent arterial chromophores. Based on the NIR absorption spectra of various biological chromophores found in human atherosclerotic arteries,[83] such a condition cannot be met at a single wavelength (i.e., $\lambda_1 = 1210$ nm) because the main absorption peak of lipids overlaps with those of other chromophores in atherosclerotic arteries such as collagen and water.[87] Instead, intrinsic suppression of those undesirable contributions can be achieved by employing the second wavelength at $\lambda_2 = \sim 970$ nm at which lipid shows barely any absorption while normal arterial chromophores exhibit similar level of absorption as at λ_1.[53–55] Against normal arterial tissue, if φ_{optical} is adjusted so that $\varphi_{\text{acoustic}}$ becomes π, and if laser powers are adjusted so that magnitudes of two resulting PA pressure become identical, the two out-of-phase PA pressure waves undergo complete destructive interference in the acoustic domain, and consequently, any undesirable contributions are highly suppressed to approximately zero baselines.[53–55] The resulting differential PA channel then becomes extremely sensitive and selective to a small trace of the spectroscopically defined target, cholesterol. This type of simultaneous dual-

wavelength modulation in differential IV-PA was shown to enhance the general imaging capability of its single-ended counterparts beyond their intrinsic limitations, but it should be emphasized that it is only feasible in PA modalities based on CW optical sources.[54,55,87]

4 Achievements

4.1 *Pulse-Based IV-PA Images*

Some early studies utilized optical sources with the wavelength around 530 nm to detect carotenoids, an organic pigment that is related to the process of lipid accumulation.[40,80–82] Within this range, Sethuraman et al.[81] reported attaining axial resolution of ~40 μm and lateral resolution of ~5.5 deg at a depth of 3 mm using a 40-MHz unfocused transducer and graphite phantom in water. Wei et al.[40] reported similar ~40 μm axial and ~480 μm lateral resolutions at a depth of 3.85 mm using a 39-MHz unfocused transducer and tungsten wires in water. However, these studies were indirect to assessing the necrotic core of a plaque and did not consider the potential effects of a blood medium on imaging parameters as most photons in this wavelength region would become strongly attenuated by hemoglobin before reaching a plaque. Following these early studies, most IV-PA systems today employ optical sources in the NIR spectral region. Even though it was not a true endoscopic system where a relatively large transducer was used to retrieve PA signals from the opposite side of a flat human artery (forward-propagation mode), Allen et al.[83] reported an image of a human aorta in the presence of blood using a 1210-nm optical source. Using a 25-MHz focused transducer, they could map the lipid distribution within the wall with ~75-μm axial and ~240-μm lateral resolutions.[83]

A single-wavelength pulse-based IV-PA system has been widely investigated for evaluation of lipid distribution in atherosclerotic plaques *ex vivo* based on distinctive absorption peaks of lipids at ~1210 and ~1720 nm. Figure 6 shows some examples of a single-wavelength pulse-based IV-PA images. In Fig. 6(a), Wang et al. generated cross-sectional IV-PA images of a section of the thoracic aorta from a specially prepared New Zealand White (NZW) rabbit using an optical parametric oscillator (OPO) tunable laser system operating at 10 Hz repetition rate, but imaging was performed at a single 1720-nm wavelength.[88] A single-element 40-MHz IVUS imaging catheter was used for PA detection and IVUS coregistration. The authors suggested that the optical absorption of lipids is stronger than that of water at 1720 nm and compared the IV-PA imaging capability in the presence of saline and rabbit whole blood. Due to the low acoustic and optical attenuation of saline, imaging depth was higher in saline compared to that in blood. Along with the corresponding histology results from hematoxylin and eosin (H&E) and oil red O (ORO), the authors concluded that their coregistered image clearly delineated regions within the arterial wall that had strong absorption at 1720 nm. Similar cross-sectional IV-PA images in Fig. 6(b) were presented by Dai et al. using a Nd:YAG pumped OPO laser at 20-Hz repetition rate with imaging wavelength fixed at 1210 nm.[42] A single-element customized 40-MHz endoscopic transducer was employed for PA detection and IVUS coregistration. A section of human artery with atherosclerotic plaques was utilized as an imaging sample. Other than IVUS and IV-PA, the authors also coregistered OCT in the combined image to help visualize the superficial structure of the vessel (i.e., fibrous cap indicated by a red arrow in the corresponding histology result), but this will not be discussed further within the scope of this review article. In comparison to the H&E histology result, the authors stated that their coregistered image mapped the plaque regions with high contrast as indicated by a green arrow.

Many efforts have also been made to validate the feasibility and performance of imaging systems *in vivo* as shown in Fig. 7. In Fig. 7(a), Wu et al.[59] generated real-time (20 FPS) cross-sectional IV-PA images of a section of the right coronary artery from a healthy farm-bred swine. In order to mimic the plaque lesion, a small piece of pork lard was delivered on a stent and the imaging catheter was directed to the area of interest through the carotid artery under guidance of angiography. Their system was

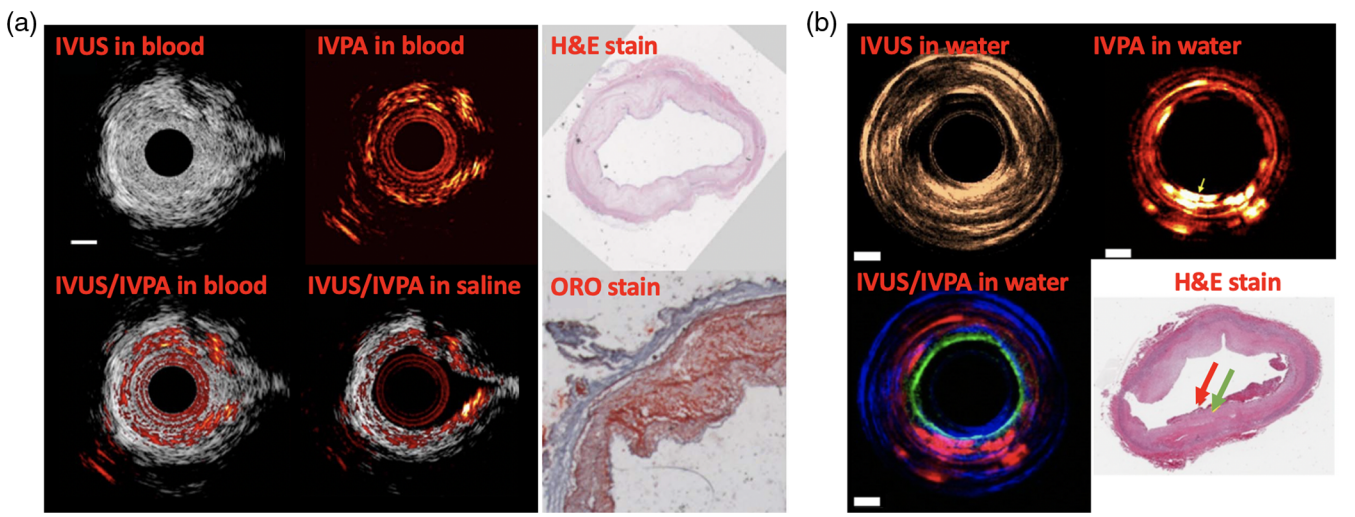

Fig. 6 Single-wavelength pulse-based IV-PA image examples generated at (a) 1720 nm and (b) 1210 nm. In (a), the white scale bar represents 1 mm in length. In (b), the white scale bars represent 2 mm in length, and the RGB codes in the combined image represent IV-PA, OCT, and IVUS, respectively. Based on the distinctive absorption coefficient peaks of lipids in NIR, pulsed optical sources at 1210 and 1720 nm were able to generate distinctive PA contrast on lipids against normal arterial wall. H&E stain, hematoxylin and eosin stain; ORO stain, oil red O stain. Reproduced with permission from Refs. 42 and 88.

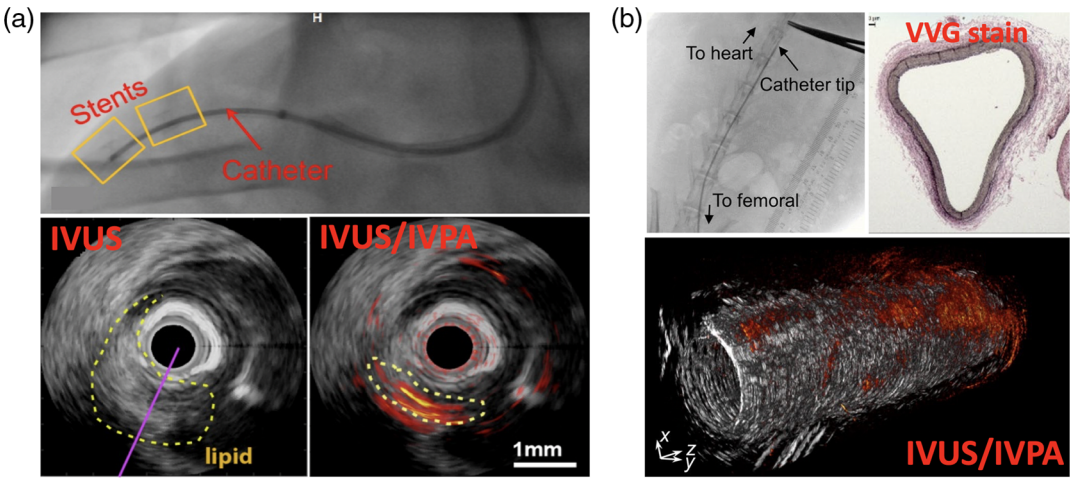

Fig. 7 Single-wavelength pulse-based IV-PA *in vivo* image examples generated from (a) swine coronary artery in saline and (b) 20-mm long rabbit thoracic aorta in blood. In both cases, optical excitation was at ~1720 and ~40-MHz single element transducers were used for PA detection and IVUS coregistration. In both examples, the presence of IV-PA catheter was visualized by x-ray angiogram. VVG stain, Verhoeff-van Gieson stain. Reproduced with permission from Refs. 59 and 60.

based on an OPO tunable laser operating at 5 kHz repetition rate at 1720 nm, and a single-element 40-MHz transducer was utilized for PA detection and IVUS coregistration. During the imaging, the artery was continuously flushed with heavy water-based saline. The authors suggested that while resulting in a good SNR of ~18 dB, their IV-PA system did not detect the entire lipid target due to the combination of catheter limitations and image processing. Cao et al. in Fig. 7(b) reported similar fast (4 to 16 FPS) *in vivo* imaging study where a three-dimensional (3-D) image of the thoracic aorta of NZW rabbit was reconstructed with axial resolution of 85 to 100 μm and lateral resolution of 170 to 450 μm.[60] The catheter was based on a Nd:YAG pumped OPO with 2-kHz repetition rate at 1730 nm and a single-element 42-MHz transducer. It was guided to the thoracic aorta via femoral artery under x-ray angiography. Due to the young age and lean diet of the rabbits used, the authors did not expect to observe any plaques, but perivascular adipose tissue. The imaging was performed under clinically relevant conditions in the presence of luminal blood. The authors suggested that their system could detect the presence of lipid within the aorta wall and perivascularly at depths greater than 4 mm. These *in vivo* studies also explored the effect of the sheath material in the resulting images.[59,60] Many polymers were tested, but the authors observed strong PA artifacts generated from the tested sheath materials when the optical beam at the selected wavelength passed through. These artifacts in many cases tent to overlap with the true PA signals from lipids and generally deteriorate image quality.

While the single-wavelength IV-PA systems could localize arterial lipids, the information was highly limited to qualitative mapping of local absorption variation. More complicated usage of pulse-based IV-PA in atherosclerosis includes multiwavelength spectroscopic imaging.[61–63] As shown in Fig. 8(a), Sethuraman et al.[84] used multispectral pulsed IV-PA imaging to distinguish various types of plaque constituents from atherosclerotic rabbit aorta. With the laser excitation wavelength range of 680 to 900 nm by a tunable pulsed Nd:YAG pumped OPO laser source and a 40-MHz coronary IVUS imaging catheter, the authors stated that different components of plaques (i.e., collagen and lipid) could be differentiated by analyzing their spectral variation (first derivative) in their absorptions. The spectral regions with different slopes were interpreted as an increase or decrease in the absorption with wavelength and were used to generate corresponding image contrasts. More intuitive multiwavelength pulsed IV-PA was reported by Allen et al. in Fig. 8(b).[83] With a fiber-coupled tunable OPO-based laser system, the authors focused on two specific wavelengths, 970 and 1210 nm. Their study showed that simple subtraction between the two independent IV-PA images generated at the abovementioned wavelengths could improve imaging specificity toward lipids by eliminating nonlipid information of plaques.

4.2 *Frequency-Swept CW-Based IV-PA and Its Differential Implementation*

While the design and assembly of a catheter was not much different from the pulse-based counterparts, one initial study on frequency-swept CW-based IV-PA was conducted on optically-transparent vessel phantoms made up of agar.[52] Some artificial absorbers, graphite and butter, were then placed within the wall of vessel phantoms to simulate atherosclerotic lipid clusters. Figure 9(a) shows the corresponding amplitude image generated by the single-wavelength IV-PA where Castelino et al. modulated a 1210-nm CW diode with 4 to 12 MHz sinusoidal chirp and used an 8.5-MHz single-element endoscopic US transducer for PA detection and IVUS coregistration.[52] This preliminary study showed the feasibility of using CW diodes and FD signal processing to construct an alternative IV-PA imager for atherosclerosis detection. Similarly, in Fig. 9(b), Lashkari et al. conducted an initial study on the differential IV-PA using a gelatin phantom where dissolved cholesterol oleate was deposited on the inner wall to mimic atherosclerotic plaques.[53] Two CW diodes at 980 and 1210 nm were simultaneously modulated by 6 to 12 MHz sinusoidal chirps with $\varphi_{\text{optical}} = 180$ deg. It should be noted that this system was not a complete catheter system as the combined light was applied from outside of the vessel phantom while a 14-MHz single-element endoscopic transducer was placed inside (forwardpropagation mode). Nevertheless, by comparing phantom amplitude images of conventional single-wavelength CW-based IV-PA

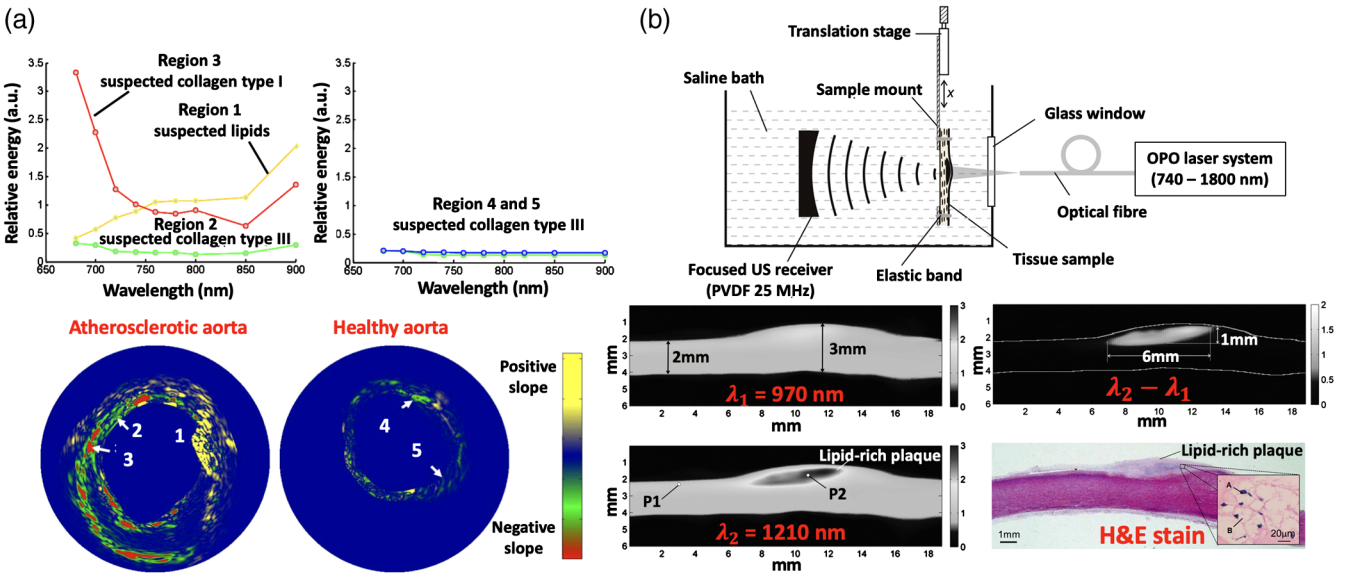

Fig. 8 Multispectral pulse-based IV-PA image examples that were generated by (a) interpreting spectral variation of different plaque constituents and (b) employing an arithmetic subtraction algorithm. P1, healthy artery region; P2, lipid-rich plaque region. Compared to the less-complex single-wavelength counterpart, multispectral approaches in general improved imaging specificity toward lipids. Reproduced with permission from Refs. 83 and 84.

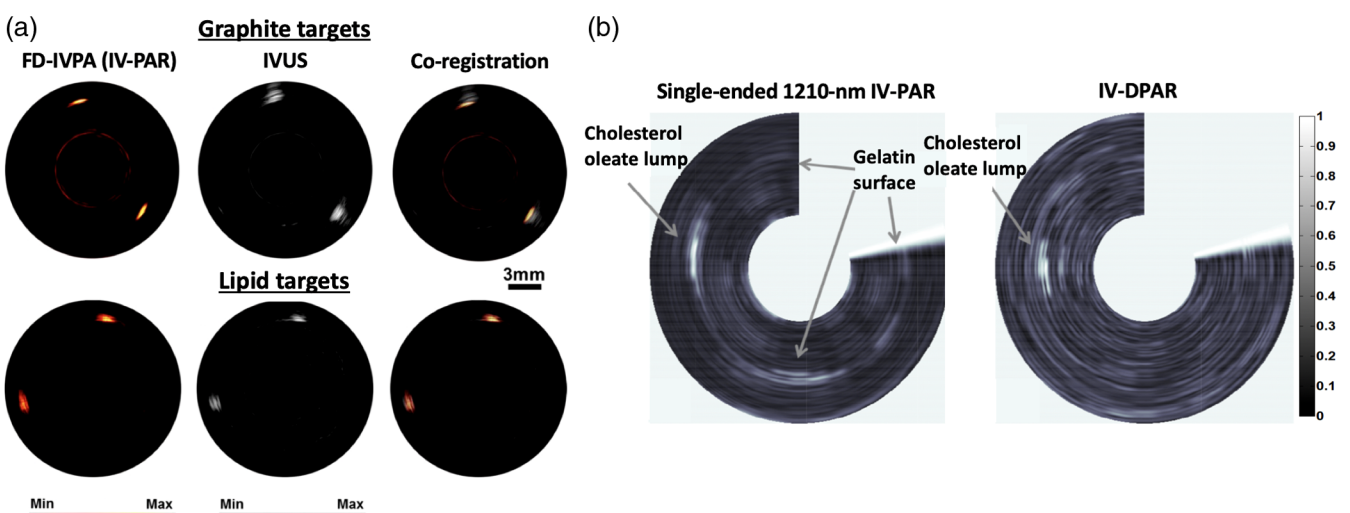

Fig. 9 Image examples of (a) 1210-nm single-wavelength frequency-swept CW-based IV-PA on graphite and butter phantoms and (b) noncatheterized 980/1210-nm dual-wavelength differential IV-PA on cholesterol phantom. Reproduced with permission from Refs. 52 and 53.

at 1210 nm and differential IV-PA, the authors demonstrated the improved cholesterol detection sensitivity and specificity in the differential modality.[53] The single-ended image showed the deposition of cholesterol oleate, but as gelatin absorbed 1210-nm light to some extent, the surface of gelatin around the phantom was also seen which could be mistaken for a fatty deposit.[53] In the corresponding differential IV-PA image, undesirable noise from gelatin was shown to be suppressed, thereby the artificial cholesterol cluster could be localized more accurately.

Very recently, further advances of the differential IV-PA have been reported. By implementing a 33-deg polished 400/440 μm (core/cladding) optical fiber, the initial differential idea was developed into a catheter system.[54,55] With recent improvements in fast modulating laser driver technology, the stability of simultaneous wavelength modulation has also improved, and consequently, the overall differential suppression procedure became more reliable.[54] Among others, optimization of various properties of optical chirp modulation, such as waveform shape and bandwidth, was shown to contribute much to further improvement of the differential imaging capability.[54] Figure 10 shows the differential IV-PA images generated from the section of early-stage human atherosclerotic aorta. Two out-of-phase CW diodes at 980 and 1210 nm were modulated by 1 to 5 MHz square chirps and a 4-MHz single-element endoscopic transducer was used for PA detection.[54] The single-ended IV-PA modes in Fig. 10(b) exhibited chemical-specific optical information, but due to the presence of strong driver-borne RF and

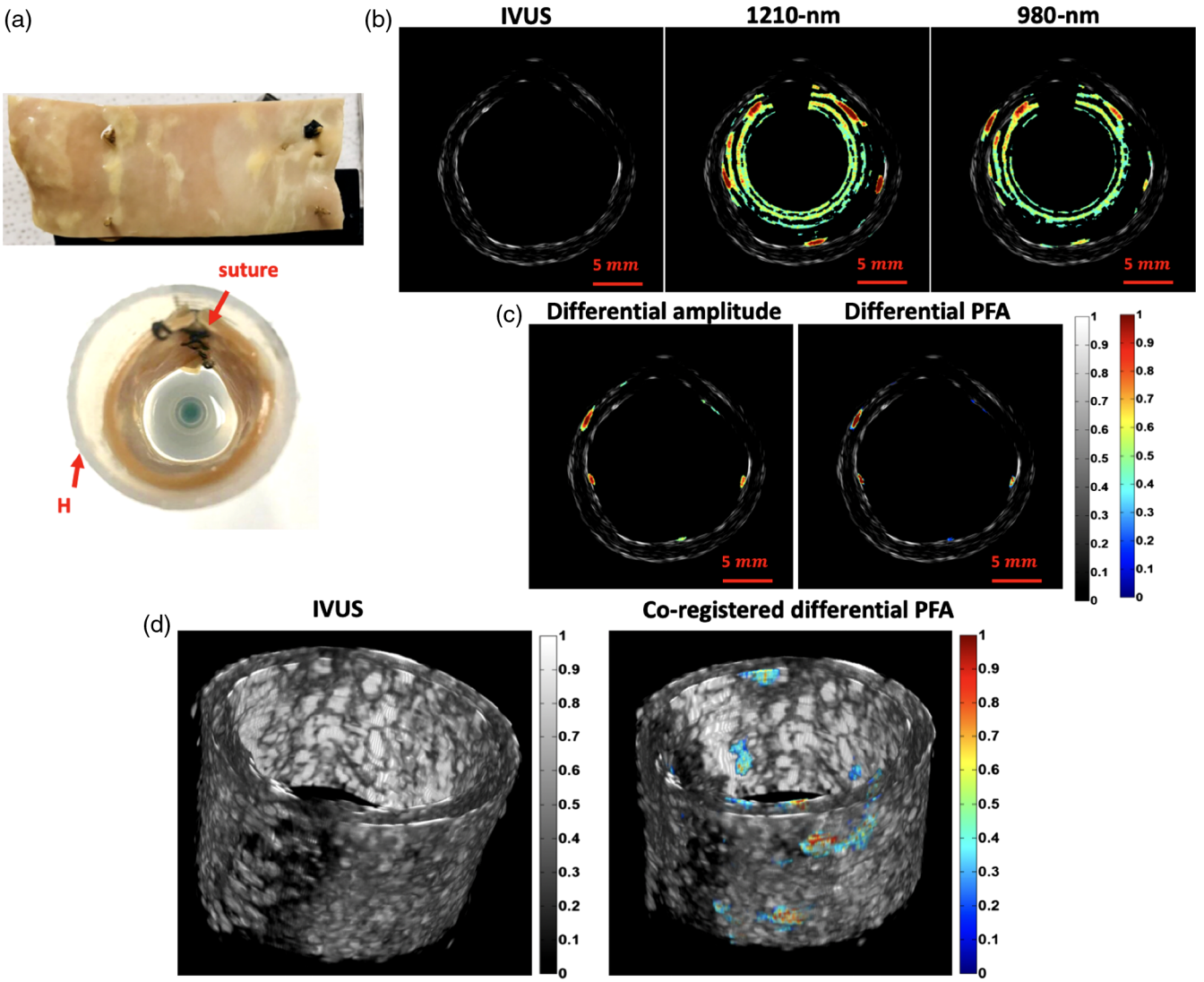

Fig. 10 (a) Picture of sutured early stage human atherosclerotic artery. (b) Cross-sectional IVUS and coregistered single-ended IV-PA/IVUS amplitude images of the early-stage human atherosclerotic artery. (c) Coregistered differential IV-PA/IVUS amplitude and PFA images of the same sample planes. (d) 3-D IVUS and coregistered 3-D differential IV-PA/IVUS PFA views of the early stage human atherosclerotic artery. H, generic plastic holder. Reproduced with permission from Ref. 54.

arterial wall noise, it was rather challenging to evaluate the true forms of plaques without any arbitrary postimage processing. In the corresponding differential IV-PA results in Fig. 10(c), the undesirable noise was suppressed prior to the detection, and the highly accurate interference-free cholesterol information could be revealed with excellent sensitivity and specificity. As expected, the PFA channel exhibited superior dynamic range to the amplitude channel, further enhancing the contrast of resulting images. The corresponding 3-D representation in Fig. 10(d) confirmed how the differential modality enables accurate detection of plaques without requiring any further analysis and interpretation. All the processing was done intrinsically and only the cholesterol information was color-coded on the image as validated by an independent histopathological study. On the other hand, since those early-stage plaque regions were not anatomically apparent, no accurate evaluation could be made in the gray-scaled IVUS images. At the tested 4-MHz modulation range, the axial resolution was relatively limited at ~380 μm. In the same study, a higher modulation of 14 MHz was also explored that could improve the resolution up to ~64 μm while compromising SNR to some extent.[54]

Unlike pulsed systems, due to the low amount of optical power exposed to the target, ~50 to 100 signal averages were required to achieve satisfactory SNR in the CW-based IV-PA in general. Assuming averages of 50 signals and 2-deg scanning resolution per plane, it takes ~9 s to generate each frame. This in turn makes it extremely challenging to translate this system for real-time evaluation of plaques. However, the authors noted that the system optical power could be safely increased by ~100% without exceeding the MPE level. While this could not be achieved with the current state-of-the-art CW diode modulation technology in the MHz range, when this is achieved in the near future, the acquisition time is expected to decrease so as to achieve >1 FPS.

5 Discussion

The field of IV-PA has been predominantly driven by pulsed optical sources and corresponding TD signal processing

methods. While such techniques were demonstrated to localize lipids based on their unique absorption signature, there are some intrinsic limitations in pulse-based IV-PA that utilize a single-ended laser. This approach provides satisfactory results when target absorbers are the major source of PA response in the region. However, its detection sensitivity, specificity, and accuracy may be severely compromised when adjacent nontarget chromophores have comparably high absorptions in those spectral regions, generating interfering PA noise. As the rarefaction-derived bipolar shape of pulsed IV-PA signals reduces the probability of differentiating between two depthwise adjacent chromophores,[49] the detection accuracy and reliability of such single-wavelength modalities are severely compromised when lipids are located adjacent to other arterial chromophores. Various forms of spectroscopic analysis have been tried with pulse-based IV-PA systems to differentiate plaques (lipids) from surrounding tissues,[39,50,83,84] but they require time-consuming sequential multiwavelength measurements for every data acquisition point and each wavelength is still evaluated independently, ignoring the possible effects of signal interferences. Many pulse-based IV-PA systems employ a multispectral approach and evaluate the arithmetic difference between the resulting PA signals to extract lipid information.[43,83] However, such multichannel processing approach in pulse-based IV-PA may not be reliable as it amplifies wideband noise along with other types of intrinsic system-induced noise (i.e., electronic noise of the transducer). Furthermore, when successive trains of ns-long pulses are applied with large temporal gaps between individual pulses, there can be no synchronous simultaneous signal processing to simply subtract noise in such multispectral PA imaging. Under time sequence conditions, any undesirable time-dependent effects interfere with actual absorber-related signals, especially in *in vivo* imaging where the imaging environment changes continuously such as with breathing motion, and thus reliable real-time imaging becomes challenging.

Recently introduced frequency-swept CW-based IV-PA modalities demonstrated their capability to generate highly informative and competitive lipid-specific IV images using low-power optical irradiation with fewer safety concerns. However, the CW-based single-wavelength approach is similarly subject to detection reliability issues as there is no single wavelength in NIR that is specifically absorbed by lipids, but not by other arterial chromophores. This is more problematic than in pulse-based counterparts as FD signal processing involves two signal components, real and imaginary. When different PA sources are adjacent to one another, their real and imaginary signals interfere independently from each other. However, as both components contribute equally to envelope formation, the multiple closely located envelope signals do not follow a simple linear interference pattern.[87] This may be reflected in the reconstructed images as false-positive (artifacts) or false-negative that could severely affect the accuracy and reliability of clinical interpretation.[55] Instead, the frequency-swept IV-PA could facilitate intrinsic differential imaging by simultaneously modulating the second wavelength. This approach may appear to be similar to multiwavelength subtraction processing in some pulse-based IV-PA systems, but it is a fundamentally different algorithm as it is independent of its individual single-ended components, thus not affected by local signal interference. Differential suppression of undesirable noise takes place in the acoustic domain upon the generation of PA pressure and the signal arriving at a detector contains only the lipid-specific information. Without any noise signals in proximity, therefore, differential IV-PA was shown to be immune to signal interference that could potentially distort the conveyed information.[54,55,87]

It should be acknowledged that the field of IV-PA has been advancing at a relatively slow rate. Numerous studies have continuously been reported that proved the technical potential of IV-PA in intravascular detection of atherosclerotic plaques under preclinical and clinically relevant conditions, but true clinical translation is still yet to be achieved. Some technical challenges that today's IV-PA systems need to resolve to accomplish clinical application include achieving $\leq$1 mm catheter size, implementing protective sheath that is transparent to optical and acoustic signals, optimizing the catheter design to maximize the overlap of optical/acoustic fields of view, and improving the light delivery systems to minimize the optical loss, among many others.[59,60] Especially in the frequency-swept CW-based IV-PA, the primary limitation of the system resides in the optical sources. While the CW beam needs to be reliably modulated in the MHz range to achieve sub-μm spatial resolution, even the current state-of-the-art optical modulators tend to have more than 50% optical power losses at the time of beam generation.[54] With extra optical losses due to fiber coupling and attenuation in the optics, the current CW-based IV-PA designs have severe efficiency problems in handling optical power. Some possible approaches for improvement may include combining multiple diodes to boost up the power and increasing signal averaging. However, these may come at extra cost in system preparation and slower image acquisition times. The optimized systems would then need to be thoroughly evaluated under true *in vivo* imaging conditions. While many *ex vivo* studies were done on human arteries and some *in vivo* animal studies were reported with artificial plaques, todays' IV-PA technology lacks experience in dealing with true atherosclerotic plaques *in vivo*, even in animal models. These technical problems would need to be successfully addressed in order to reach the clinical translation of IV-PA imaging.

6 Summary

The field of medical PA imaging has been advancing to optically differentiate a variety of bioabnormalities such as tumors with acoustic depth and resolution, but it has been highly dominated by pulse-based systems based on high-power optical sources and computationally efficient TD signal processing methods. As an alternative, the FD method based on frequency-swept CW optical sources started to appear in the field in mid 2000s. For relatively large-scale imaging using phantoms, the frequency-swept CW-based PA methods have been demonstrated to be highly competitive to their pulse-based counterpart in terms of imaging depth, SNR, and resolution while utilizing compact, robust, and much less expensive CW laser diodes with low power optical irradiation. Most importantly, waveform engineering techniques, such as wavelength modulation and pulse compression that are unique to CW-based PA, have demonstrated advantages including signal dynamic range enhancement and background elimination, boosting diagnostic specificity of absorbing tissues such as blood oxygenation.

As a recent add-on to the field of IV atherosclerosis imaging, IV-PA is a unique imaging modality that can provide optically derived compositional information of diseased tissues with acoustic depth resolution. As shown in many biomedical applications, pulse-based IV-PA has been leading the development of this technique and some promising preclinical results have been

reported. Single-wavelength-pulsed optical sources with high peak power can induce excellent PA contrast on lipids but various multispectral approaches have also been investigated in order to extract quantitative information from atherosclerotic tissues. The alternative IV-PA technique based on CW optical excitation has also been introduced. Despite its low optical power, this modality has demonstrated imaging performance quite similar to its pulsed counterpart with regard to its chemical-specific imaging capability by implementing radar-like FD signal processing algorithms. The use of CW irradiation allows more flexible simultaneous multispectral PA modulation, resulting in the unique differential PA channel that is exceptionally sensitive and selective to the spectroscopically defined imaging targets. Overall, IV-PA research, either pulse- or CW-based, has been reporting highly promising preclinical applications. With intuitive coregistration with clinically acceptable IVUS or OCT, IV-PA is expected to further enhance the accuracy and reliability of imaging-based evaluation of atherosclerosis. Many attempts are being made to translate IV-PA modalities into clinical applications in regard to imaging time, cost, size, and safety, among other factors. While much more preclinical/clinical research remains to follow, the unique imaging capability of IV-PA holds strong diagnostic potential for atherosclerosis.

Disclosures

Authors declare no conflicts of interest.

Acknowledgments

SS. S. C. gratefully acknowledges the support of the Natural Sciences and Engineering Research Council of Canada (NSERC) for an Alexander Graham Bell Canada Graduate Scholarships–Doctoral (CGS-D) and the government of Ontario for a Queen Elizabeth II Graduate Scholarship in Science and Technology (QEII-GSST). A.M. acknowledges an NSERC Discovery award, the Canada Research Chairs Program, and a University of Toronto Connaught Award.

References

1. R. J. Jones, Ed., *Evolution of the Atherosclerotic Plaque*, University of Chicago Press, Chicago, Illinois (1963).
2. C. P. Sparrow and J. Olszewski, "Cellular oxidation of low density lipoprotein is caused by thio production in media containing transition metal ions," *J. Lipid Res.* **34**(7), 1219–1228 (1993).
3. R. Virmani et al., "Lessons from sudden coronary death: a comprehensive morphological classification scheme for atherosclerotic lesions," *Arterioscl. Throm. Vasc. Biol.* **20**(5), 1262–1275 (2000).
4. P. Libby, P. M. Ridker, and A. Maseri, "Inflammation and atherosclerosis," *Circulation* **105**(9), 1135–1143 (2002).
5. P. K. Shah, "Mechanisms of plaque vulnerability and rupture," *J. Am. Coll. Cardiol.* **41**(4), S15–S22 (2003).
6. P. A. Price, S. A. Faus, and M. K. Williamson, "Warfarin-induced artery calcification is accelerated by growth and vitamin D," *Arterioscl. Throm. Vasc. Biol.* **20**(2), 317–327 (2000).
7. J. D. Miller, "Cardiovascular calcification: orbicular origins," *Nat. Mater.* **12**(6), 476–478 (2013).
8. Y. Nemerson, "A simple experiment and a weakening paradigm: the contribution of blood to propensity for thrombus formation," *Arterioscl. Throm. Vasc. Biol.* **22**(9), 1369–1369 (2002).
9. D. C. Levin and J. T. Fallon, "Significance of the angiographic morphology of localized coronary stenosis: histopathologic correlations," *Circulation* **66**(2), 316–320 (1982).
10. E. Falk, "Plaque rupture with severe pre-existing stenosis precipitating coronary thrombosis. Characteristics of coronary atherosclerotic plaques underlying fatal occlusive thrombi," *Br. Heart J.* **50**(2), 127–134 (1983).
11. M. J. Davies and A. Thomas, "Thrombosis and acute coronary-artery lesions in sudden cardiac ischemic death," *New Engl. J. Med.* **310**(18), 1137–1140 (1984).
12. A. P. Burke et al., "Coronary risk factors and plaque morphology in men with coronary disease who died suddenly," *New Engl. J. Med.* **336**(18), 1276–1282 (1997).
13. J. A. Ambrose et al., "Angiographic morphology and the pathogenesis of unstable angina pectoris," *J. Am. Coll. Cardiol.* **5**(3), 609–616 (1985).
14. E. Falk, P. K. Shah, and V. Fuster, "Coronary plaque disruption," *Circulation* **92**(3), 657–671 (1995).
15. G. Brown et al., "Regression of coronary artery disease as a result of intensive lipid-lowering therapy in men with high levels of apolipoprotein B," *New Engl. J. Med.* **323**(19), 1289–1298 (1990).
16. D. Giroud et al., "Relation of the site of acute myocardial infarction to the most sever coronary arterial stenosis at prior angiography," *Am. J. Cardiol.* **69**(8), 729–732 (1992).
17. P. Schoenhagen et al., "Extent and direction of arterial remodeling in stable versus unstable coronary syndromes: an intravascular ultrasound study," *Circulation* **101**(6), 598–603 (2000).
18. C. von Birgelen et al., "Plaque distribution and vascular remodeling of ruptured and nonruptured coronary plaques in the same vessel: an intravascular ultrasound study in vivo," *J. Am. Coll. Cardiol.* **37**(7), 1864–1870 (2001).
19. M. Takano et al., "Mechanical and structural characteristics of vulnerable plaques: analysis by coronary angioscopy and intravascular ultrasound," *J. Am. Coll. Cardiol.* **38**(1), 99–104 (2001).
20. H. M. Loree et al., "Effects of fibrous cap thickness on peak circumferential stress in model atherosclerotic vessels," *Circ. Res.* **71**(4), 850–858 (1992).
21. J. E. Muller, "Morning increase of onset of myocardial infarction. Implications concerning triggering events," *Cardiology* **76**(2), 96–104 (1989).
22. S. N. Willich et al., "Sudden cardiac death. Support for a role of triggering in causation," *Circulation* **87**(5), 1442–1450 (1993).
23. J. E. Muller, "Triggering of cardiac events by sexual activity: findings from a case-crossover analysis," *Am. J. Cardiol.* **86**(2A), 14F–18F (2000).
24. J. A. Goldstein et al., "Multiple complex coronary plaques in patients with acute myocardial infarction," *New Engl. J. Med.* **343**(13), 915–922 (2000).
25. J. M. Tarkin et al., "Imaging atherosclerosis," *Circ. Res.* **118**(4), 750–769 (2016).
26. F. R. Joshi et al., "Non-invasive imaging of atherosclerosis," *Eur. Heart J.-Cardiovasc. Imaging* **13**(3), 205–218 (2012).
27. G. N. Hounsfield, "Computerized transverse axial scanning (tomography). 1. Description of system," *Br. J. Radiol.* **46**(552), 1016–1022 (1973).
28. World Health Organization, "Training in diagnostic ultrasound: essentials, principles and standards," *WHO Technical Report Series 875* (1998).
29. F. Aaron and D. B. Downey, "3-D ultrasound imaging: a review," *IEEE Eng. Med. Biol.* **15**(6), 41–51 (1996).
30. A. Nair et al., "Automated coronary plaque characterisation with intravascular ultrasound backscatter: ex vivo validation," *EuroIntervention* **3**(1), 113–120 (2007).
31. T. Thim et al., "Unreliable assessment of necrotic core by virtual histology intravascular ultrasound in porcine coronary artery disease," *Circ-Cardiovasc. Imaging* **3**(4), 384–391 (2010).
32. E. S. Shin et al., "In vivo findings of tissue characteristics using iMap IVUS and Virtual Histology IVUS," *EuroIntervention* **6**(8), 1017–1019 (2011).
33. J. G. Fujimoto et al., "Optical coherence tomography: an emerging technology for biomedical imaging and optical biopsy," *Neoplasia* **2**(1–2), 9–25 (2000).
34. H. Yabushita et al., "Characterization of human atherosclerosis by optical coherence tomography," *Circulation* **106**(13), 1640–1645 (2002).
35. A. G. Bell, "On the production and reproduction of sound by light," *Am. J. Sci.* **20**(118), 305–324 (1880).
36. C. Tsai, J. Chen, and W. Wang, "Near-infrared absorption property of biological soft tissue constituents," *J. Med Biol. Eng.* **21**(1), 7–13 (2001).

37. R. R. Anderson et al., "Selective photothermolysis of lipid-rich tissues: a free electron laser study," *Laser. Surg. Med.* **38**(10), 913–919 (2006).
38. J. D. Caplan et al., "Near-infrared spectroscopy for the detection of vulnerable coronary artery plaques," *J. Am. Coll. Cardiol.* **47**(8), C92–C96 (2006).
39. K. Jansen et al., "Photoacoustic imaging of human coronary atherosclerosis in two spectral bands," *Photoacoustics* **2**(1), 12–20 (2014).
40. W. Wei et al., "Integrated ultrasound and photoacoustic probe for co-registered intravascular imaging," *J. Biomed. Opt.* **16**(10), 106001 (2011).
41. J.-M. Yang et al., "Simultaneous functional photoacoustic and ultrasonic endoscopy of internal organs in vivo," *Nat. Med.* **18**(8), 1297–1302 (2012).
42. X. Dai et al., "Miniature endoscope for multimodal imaging," *ACS Photonics* **4**, 174–180 (2017).
43. S. Shang et al., "Simultaneous imaging of atherosclerotic plaque composition and structure with dual-mode photoacoustic and optical coherence tomography," *Opt. Express* **25**(2), 530–539 (2017).
44. A. C. Tam, "Applications of photoacoustic sensing techniques," *Rev. Mod. Phys.* **58**(2), 381–431 (1986).
45. C. Dunsby and P. M. W. French, "Techniques for depth-resolved imaging through turbid media including coherent-gated imaging," *J. Phys. D. Appl. Phys.* **36**(14), R207–R227 (2003).
46. F. Liu, K. M. Yoo, and R. R. Alfano, "Transmitted photon intensities through biological tissues within various time windows," *Opt. Lett.* **19**(10), 740–742 (1994).
47. Y. Pu et al., "Determination of optical coefficients and fractal dimensional parameters of cancerous and normal prostate tissues," *Appl. Spectrosc.* **66**(7), 828–834 (2012).
48. B. Lashkari and A. Mandelis, "Linear frequency modulation photoacoustic radar: Optimal bandwidth and signal-to-noise ratio for frequency-domain imaging of turbid media," *J. Acoust. Soc. Am.* **130**(3), 1313–1324 (2011).
49. B. Lashkari and A. Mandelis, "Comparison between pulsed laser and frequency-domain photoacoustic modalities: signal-to-noise ratio, contrast, resolution, and maximum depth detectivity," *Rev. Sci. Instrum.* **82**(9), 094903 (2011).
50. K. Jansen et al., "Spectroscopic intravascular photoacoustic imaging of lipids in atherosclerosis," *J. Biomed. Opt.* **19**(2), 026006 (2014).
51. D. Vander Laan et al., "Real-time intravascular ultrasound and photoacoustic imaging," *IEEE Trans. Ultrason. Ferroelectr. Freq. Control.* **64**(1), 141–149 (2017).
52. R. F. Castelino et al., "Combined frequency domain photoacoustic and ultrasound imaging for intravascular applications," *Biomed. Opt. Express* **7**(11), 4441–4449 (2016).
53. B. Lashkari et al., "Characterization of an intraluminal differential frequency-domain photoacoustic system," *Proc. SPIE* **9708**, 970808 (2016).
54. SS. S. Choi et al., "Interference-free detection of lipid-laden atherosclerotic plaques by 3D co-registration of frequency-domain differential photoacoustic and ultrasound radar imaging," submitted (2019).
55. SS. S. Choi et al., "Frequency-domain differential photoacoustic radar: theory and validation for ultra-sensitive atherosclerotic plaque imaging," *J. Biomed. Opt.* **24**(6), 066003 (2019).
56. J. Hui et al., "Real-time intravascular photoacoustic-ultrasound imaging of lipid-laden plaque in human coronary artery at 16 frames per second," *Sci. Rep.* **7**, 1417 (2017).
57. P. Wang et al., "Intravascular tri-modality system: combined ultrasound, photoacoustic and elasticity imaging," *Appl. Phys. Lett.* **113**, 253701 (2018).
58. K. Xiong et al., "Autofocusing optical-resolution photoacoustic endoscopy," *Opt. Lett.* **43**(8), 1846–1849 (2018).
59. M. Wu et al., "Real-time volumetric lipid imaging in vivo by intravascular photoacoustics at 20 frames per second," *Biomed. Opt. Express* **8**(2), 943–953 (2017).
60. Y. Cao et al., "Fast assessment of lipid content in arteries in vivo by intravascular photoacoustic tomography," *Sci. Rep.* **8**, 2400 (2018).
61. V. Ntziachristos et al., "Looking and listening to light: the evolution of whole-body photonic imaging," *Nat. Biotechnol.* **23**(30), 313–320 (2005).
62. P. Beard, "Biomedical photoacoustic imaging," *Interface Focus* **1**(4), 602–631 (2011).
63. R. A. Kruger, D. R. Reinecke, and G. A. Kruger, "Thermoacoustic computed tomography-technical considerations," *Med. Phys.* **26**(9), 1832–1837 (1999).
64. C. G. A. Hoelen and F. F. M. de Mul, "Image reconstruction for photoacoustic scanning of tissue structures," *Appl. Opt.* **39**(31), 5872–5883 (2000).
65. M. Xu, Y. Xu, and L. V. Wang, "Time-domain reconstruction algorithms and numerical simulations for thermoacoustic tomography in various geometries," *IEEE Trans. Bio-Med. Eng.* **50**(9), 1086–1099 (2003).
66. T. Sowers et al., "Laser threshold and cell damage mechanism for intravascular photoacoustic imaging," *Laser Surg. Med.* **51**, 466–474 (2019).
67. S. Telenkov et al., "Frequency-domain photothermoacoustics: alternative imaging modality of biological tissues," *Appl. Phys.* **105**(10), 102029 (2009).
68. S. Telenkov and A. Mandelis, "Fourier-domain biophotoacoustic subsurface depth selective amplitude and phase imaging of turbid phantoms and biological tissue," *J. Biomed. Opt.* **11**(4), 044006 (2006).
69. K. Maslov and L. V. Wang, "Photoacoustic imaging of biological tissue with intensity-modulated continuous-wave laser," *J. Biomed. Opt.* **13**(2), 024006 (2008).
70. Y. Fan et al., "Development of a laser photothermoacoustic frequency-swept system for subsurface imaging: theory and experiments," *J. Acoust. Soc. Am.* **116**(6), 3523–3533 (2004).
71. B. Lashkari and A. Mandelis, "Photoacoustic radar imaging signal-to-noise ratio, contrast, and resolution enhancement using nonlinear chirp modulation," *Opt. Lett.* **35**(10), 1623–1625 (2010).
72. S. Telenkov and A. Mandelis, "Photothermoacoustic imaging of biological tissue: maximum depth characterization comparison of time and frequency-domain measurements," *J. Biomed. Opt.* **14**(4), 044025 (2009).
73. G. Langer et al., "Frequency domain photoacoustic and fluorescence microscopy," *Biomed. Opt. Express* **7**(7), 2692–2702 (2016).
74. P. Mohajerani, S. Kellnberger, and V. Ntziachristos, "Frequency domain optoacoustic tomography using amplitude and phase," *Photoacoustics* **2**(3), 111–118 (2014).
75. S. Kellnberger et al., "Optoacoustic microscopy at multiple discrete frequencies," *Light-Sci. Appl.* **7**, 109 (2018).
76. A. Petschke and P. J. La Riviere, "Comparison of photoacoustic imaging systems using continuous-wave lasers with a chirped intensity modulation frequency to pulsed lasers," *Proc. SPIE* **7899**, 78992O (2011).
77. S.-Y. Su and P.-C. Li, "Photoacoustic generation using coded excitation," *Proc. SPIE* **7899**, 789927 (2011).
78. P. LeBoulluec, H. Liu, and B. Yuan, "A cost-efficient frequency-domain photoacoustic imaging system," *Am. J. Phys.* **81**(9), 712–717 (2013)
79. K. Jnawali et al., "Photoacoustic simulation study of chirp excitation response from different size absorbers," *Proc. SPIE* **10139**, 101391L (2017).
80. P. C. Beard and T. N. Mills, "Characterization of post mortem arterial tissue using time-resolved photoacoustic spectroscopy at 436, 461 and 532 nm," *Phys. Med. Biol.* **42**(1), 177–198 (1997).
81. S. Sethuraman et al., "Intravascular photoacoustic imaging using an IVUS imaging catheter," *IEEE Trans. Ultrason. Ferroelectr. Freq. Control* **54**(5), 978–986 (2007).
82. J.-M. Yang et al., "Photoacoustic endoscopy," *Opt. Lett.* **34**(10), 1591–1593 (2009).
83. T. J. Allen et al., "Spectroscopic photoacoustic imaging of lipid-rich plaques in the human aorta in the 740 to 1400 nm wavelength range," *J. Biomed. Opt.* **17**(6), 061209 (2012).
84. S. Sethuraman et al., "Spectroscopic intravascular photoacoustic imaging to differentiate atherosclerotic plaques," *Opt. Express* **16**(5), 3362–3367 (2008).
85. S. Telenkov, R. Alwi, and A. Mandelis, "Photoacoustic correlation signal-to-noise ratio enhancement by coherent averaging and optical waveform optimization," *Rev. Sci. Instrum.* **84**(10), 104907 (2013).
86. B. Lashkari et al., "Frequency-domain photoacoustic phase spectroscopy: a fluence-independent approach for quantitative probing of hemoglobin oxygen saturation," *IEEE J. Sel. Top. Quantum Electron.* **22**(3), 6801010 (2015).
87. SS. S. Choi et al., "Frequency-domain differential photoacoustic radar: theory and simulation for ultra-sensitive cholesterol imaging," *Proc. SPIE* **10878**, 1087812 (2019).

88. B. Wang et al., "Intravascular photoacoustic imaging of lipid in atherosclerotic plaques in the presence of luminal blood," *Opt. Lett.* **37**(7), 1244–1246 (2012).

Sung Soo Sean Choi is a PhD candidate at the University of Toronto. He received his MASc degree in biomedical engineering from the University of Toronto in 2015 and his BSc degree in biomedical sciences from the University of Waterloo in 2012. His research interest is in developing innovative medical imaging technology for early disease detection. He is a student member of SPIE.

Andreas Mandelis is a full professor of mechanical and industrial engineering; electrical and computer engineering; and the Institute of Biomaterials and Biomedical Engineering, University of Toronto, and director of the Center for Advanced Diffusion-Wave and Photoacoustic Technologies at the University of Toronto. He has published more than 400 scientific papers in refereed journals and 190 proceedings papers. He has received numerous national and international prizes and awards and has several patents in biothermophotonics and biophotoacoustic tissue imaging.